

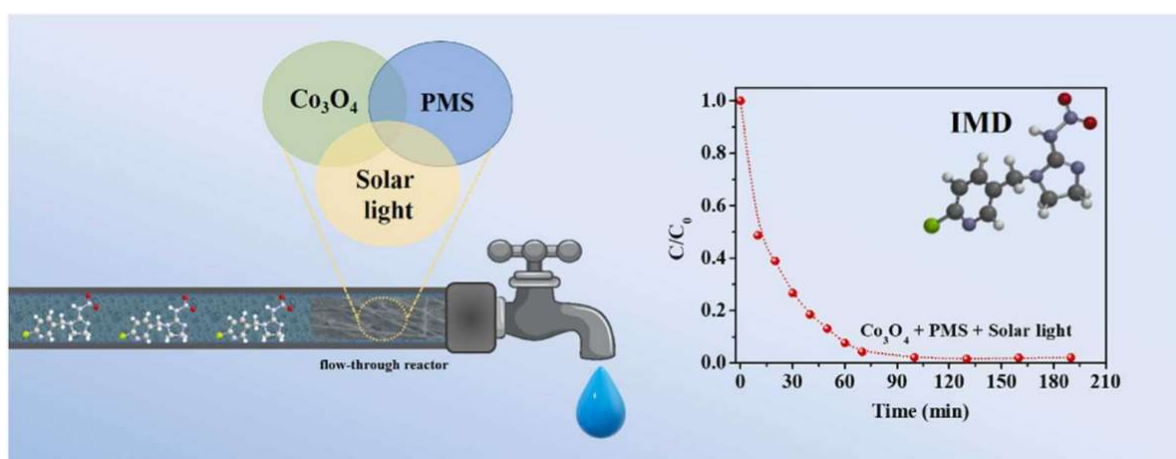
# Peroxymonosulfate activation by $\text{Co}_3\text{O}_4$ coatings for imidacloprid degradation in a continuous flow-cell reactor under simulated solar irradiation

Submitted version made available in agreement with publisher's policy.

Please, cite as follows:

Roberta R.M. Silva, Laura Valenzuela, Roberto Rosal, Luís A.M. Ruotolo, Francisco G.E. Nogueira, Ana Bahamonde. Peroxymonosulfate activation by  $\text{Co}_3\text{O}_4$  coatings for imidacloprid degradation in a continuous flow-cell reactor under simulated solar irradiation. *Journal of Environmental Chemical Engineering*, Volume 11, Issue 2, 109265, 2023

<https://doi.org/10.1016/j.jece.2023.109265>



<https://www.sciencedirect.com/science/article/pii/S2213343723000040>

# Peroxymonosulfate activation by Co<sub>3</sub>O<sub>4</sub> coatings for imidacloprid degradation in a continuous flow-cell reactor under simulated solar irradiation

Roberta R.M. Silva<sup>1,\*</sup>, Laura Valenzuela<sup>2</sup>, Roberto Rosal<sup>2</sup>, Luís A.M. Ruotolo<sup>1</sup>, Francisco G.E. Nogueira<sup>1</sup>, Ana Bahamonde<sup>3</sup>

<sup>1</sup> Department of Chemical Engineering, Federal University of São Carlos, Rod. Washington Luiz, km 235, São Carlos, SP 13565-905, Brazil

<sup>2</sup> Department of Chemical Engineering, University of Alcalá, Alcalá de Henares, Madrid E-28871, Spain

<sup>3</sup> Instituto de Catálisis y Petroleoquímica, ICP-CSIC, Marie Curie 2, 28049 Madrid, Spain

\* Corresponding author: robertamacieel@gmail.com

## Abstract

In this work, a Co<sub>3</sub>O<sub>4</sub> coating prepared by precipitation and vacuum filtration was applied to photoactivate peroxymonosulfate (PMS), for the degradation of imidacloprid (IMD) under continuous-flow conditions. The effects of PMS concentration, flow rate, and type of irradiation were evaluated. Under optimal conditions (0.2 g<sub>PMS</sub> L<sup>-1</sup>, 0.1 mL min<sup>-1</sup>, and simulated solar irradiation), 99% IMD photodegradation was achieved after 2 h of operation. The outstanding performance of the Co<sub>3</sub>O<sub>4</sub>/PMS/solar irradiation process was attributed to the synergistic activation of PMS by Co<sup>2+</sup> and Co<sup>3+</sup> species in the Co<sub>3</sub>O<sub>4</sub> catalyst and the UV component of solar irradiation, in either the homogeneous phase or following the adsorption of PMS onto Co<sub>3</sub>O<sub>4</sub>. Quenching experiments revealed that sulfate and superoxide radicals, as well as singlet oxygen, were the main active species responsible for IMD oxidation. Measurements using HPLC-high resolution mass spectrometry enabled the identification of eight intermediate products, allowing the proposal of a degradation pathway. The combination of solar light, Co<sub>3</sub>O<sub>4</sub>, and PMS is a simple and low-cost approach with the potential to treat effluents containing harmful pollutants.

Keywords: Cobalt oxide; Peroxymonosulfate; Solar irradiation; Continuous operation; Imidacloprid

## 1. Introduction

Imidacloprid (IMD), 1-(6-chloro-3-pyridylmethyl)-N-nitroimidazolidin-2-ylideneamine, is a neonicotinoid pesticide commonly used for the control of insect pests such as aphids, fleas, termites, whiteflies, turf and soil insects, and some beetles [1]. The main uses of IMD include agricultural, veterinary, and domestic applications [2]. Due to its broad-spectrum characteristics, high insecticidal activity, and long-term effectiveness, imidacloprid became the largest selling insecticide and the second largest selling pesticide worldwide in 2008 [3]. However, the massive use of IMD in agricultural and urban areas, its low volatility and biodegradability, and high solubility and stability in water [2] create a potential risk of water contamination when it is transported to surface waters in runoff or is leached into groundwater after application [4]. Numerous monitoring studies conducted over the last few years have confirmed this concern, since IMD has been detected in surface waters at concentrations up to 320 µg L<sup>-1</sup> [2, 5-7]. At concentrations below 1.0 µg L<sup>-1</sup>, IMD has chronic effects on aquatic insects, while acute toxicity is reached at below 20 µg L<sup>-1</sup> in nontarget organisms including *Hyalella azteca*, ostracods, and *Chironomus riparius* [8]. Moreover, IMD may cause severe sublethal effects in vertebrate animals (some

mammals, birds, and fishes), such as reduced growth and reproductive rates, impaired nervous system and immune function, weakened mobility, disturbed metabolic balance, and DNA damage [4]. Despite its detectable concentrations in water bodies have been ranged from ng L<sup>-1</sup> to µg L<sup>-1</sup>, several previous works focused their studies on high concentrations (3–40 mg L<sup>-1</sup>) IMD removal, which was due to either analytical method limitations to accurately quantify very low concentration levels or the fact that IMD is currently not regulated by legislation in many countries [9-12].

Because of its persistent character, IMD cannot be efficiently removed using conventional techniques in municipal wastewater treatment plants. In this regard, advanced oxidation processes (AOPs) based on sulfate radicals (SO<sub>4</sub><sup>•-</sup>) have recently gained attention from the scientific community and have been investigated for the degradation of several organic compounds [13-15], including IMD [10]. The sulfate radical is a powerful oxidant that can be generated by scission of the peroxy bond of peroxymonosulfate (PMS, HSO<sub>5</sub><sup>-</sup>) upon activation. Compared to traditional hydroxyl radical-based AOPs (redox potential of 1.8–2.7 V vs. NHE and half-life of 20 ns), SO<sub>4</sub><sup>•-</sup> can present similar or even higher redox potential (2.5–3.1 V vs. NHE), together with a longer half-life (30–40 µs), in a wider working

pH range (2–8) [16]. PMS can be activated by heat, ultrasound, ultraviolet irradiation, transition metals (homogeneous and heterogeneous), electrons of a semiconductor conduction band, or carbon catalysts [16]. Transition metals are usually preferred, due to their abundance and efficient activation of PMS to produce  $\text{SO}_4^{\cdot-}$ , resulting from their ability to transfer charge between different valence states [17]. Among them, the cobalt ion ( $\text{Co}^{2+}$ ) is regarded the most effective [18]. However, its toxic nature causes secondary water pollution, which limits its practical application in homogeneous catalysis for water and wastewater treatment [19]. Therefore, it is necessary to use heterogeneous systems. To this end, cobalt-based catalysts such as  $\text{Co}_3\text{O}_4$  have been investigated, in order to avoid  $\text{Co}^{2+}$  contamination while promoting PMS activation, as reported by Dionysiou et al. [20] for 2,4-dichlorophenol degradation using  $\text{Co}_3\text{O}_4$  at neutral pH. The stability of  $\text{Co}_3\text{O}_4$  was also reported by Chen et al. [21] and Hu et al. [17].

$\text{Co}_3\text{O}_4$  is not only an effective catalyst for PMS activation but is also a visible light-driven photocatalyst. Therefore, when the  $\text{Co}_3\text{O}_4$ /PMS system is illuminated with solar irradiation, the cobalt species in  $\text{Co}_3\text{O}_4$  and the electrons in its conduction band can simultaneously activate PMS for the generation of sulfate radicals and other reactive oxygen species (ROS) [22]. Although the catalytic and photocatalytic activation of PMS by  $\text{Co}_3\text{O}_4$  has already been investigated, only batch degradation has been considered until now. To the best of our knowledge, there are no reports concerning the performance of  $\text{Co}_3\text{O}_4$ /PMS for the degradation of organic pollutants in a continuous system, employing an immobilized catalyst illuminated by solar irradiation. We believe that this is a promising strategy that can overcome the challenges associated with the use of suspended powder catalysts requiring laborious separation operations after the treatment.

In the present work, the photochemical activation of PMS by  $\text{Co}_3\text{O}_4$  and solar light was investigated, for the first time, for the degradation of IMD in a continuous flow system. In order to achieve high degradation rates, the effects of PMS concentration, flow rate, and type of irradiation were investigated to determine the optimized operational condition. The mechanism of IMD degradation in the  $\text{Co}_3\text{O}_4$ /PMS/solar irradiation system was investigated using quenching experiments. Measurements by HPLC-high resolution mass spectrometry were used to identify the reaction intermediates and propose a degradation pathway.

## 2. Experimental

### 2.1. Reagents

Ammonium bicarbonate ( $\text{NH}_4\text{HCO}_3$ ,  $\geq 99.5\%$ ), peroxymonosulfate (PMS,  $\text{KHSO}_5 \cdot 0.5\text{KHSO}_4 \cdot 0.5\text{K}_2\text{SO}_4$ ,  $\geq 95.0\%$ ) and sodium azide ( $\text{NaN}_3$ ,  $99.0\%$ ) were purchased from Sigma-Aldrich. Cobalt (II) nitrate

hexahydrate ( $\text{Co}(\text{NO}_3)_2 \cdot 6\text{H}_2\text{O}$ ), methanol (MeOH,  $\text{CH}_3\text{OH}$ , HPLC grade), acetonitrile ( $\text{CH}_3\text{CN}$ , HPLC grade), tert-butyl alcohol (TBA,  $\text{C}_4\text{H}_{10}\text{O}$ ,  $99.0\%$ ), and p-benzoquinone (p-BQ,  $\text{C}_6\text{H}_4\text{O}_2$ ,  $> 99.5\%$ ) were supplied by Merck, Honeywell, Scharlau, Panreac, and Fluka Analytical, respectively. Technical grade imidacloprid (IMD,  $97.9\%$ ) was obtained from Bayer Hispania S.A. (Spain). All chemicals were used as received.

### 2.2. Synthesis and characterization of $\text{Co}_3\text{O}_4$ nanoparticles

$\text{Co}_3\text{O}_4$  nanoparticles (NPs) were obtained by precipitation followed by calcination, similar to the synthesis described elsewhere [23]. Briefly, 1.81 g of  $\text{Co}(\text{NO}_3)_2 \cdot 6\text{H}_2\text{O}$  was dissolved in a solution containing 70 mL of ethanol and 170 mL of ultrapure water, to which 1.49 g of  $\text{NH}_4\text{HCO}_3$  was added, under stirring at room temperature. After 4 h, the purple precipitate formed was collected by centrifugation, washed with distilled water and ethanol, and dried overnight at  $50^\circ\text{C}$ . The solid was calcined in air at  $400^\circ\text{C}$  for 2 h, forming a black cobalt oxide powder.

The crystal structure of the  $\text{Co}_3\text{O}_4$  was characterized by X-ray diffraction (XRD, PANalytical X'Pert Pro), using  $\text{Cu K}\alpha$  radiation, and the crystallite size was estimated according to the Scherrer equation. Dynamic particle size and zeta potential ( $\zeta$ -potential) measurements were performed by dynamic light scattering (DLS) at  $25^\circ\text{C}$ , using a Malvern Zetasizer Nano ZS instrument. The textural structure of the catalyst was investigated by acquisition of  $\text{N}_2$  adsorption-desorption isotherms at  $-196^\circ\text{C}$ , using a Micromeritics ASAP 2420 instrument, with the sample previously degassed overnight at  $140^\circ\text{C}$  to a residual pressure of  $< 10^{-4}$  Pa. The specific surface area ( $S_{\text{BET}}$ ) was determined using the Brunauer-Emmett-Teller (BET) equation. The micropore volume and the external or non-microporous surface were analyzed by the t-method. The optical properties of the oxide were investigated by UV-Vis diffuse reflectance spectroscopy (DRS), using an Agilent Cary 5000 instrument.

### 2.3. Fabrication and characterization of $\text{Co}_3\text{O}_4$ coatings

The  $\text{Co}_3\text{O}_4$  coating was produced by a simple vacuum filtration method. The  $\text{Co}_3\text{O}_4$  powder (50 mg) was dispersed in 100 mL of ultrapure water and homogenized for 30 min using an ultrasonic processor (Bioblock Scientific). The suspension (10 mL) was vacuum filtered onto a glass microfiber filter (Whatman,  $1\ \mu\text{m}$  pore size, 47 mm diameter). The  $\text{Co}_3\text{O}_4$  coating ( $0.4\ \text{mg cm}^{-2}$ ) was dried overnight at  $100^\circ\text{C}$ . The morphologies of the as-fabricated catalytic surfaces were observed by scanning electron microscopy (SEM, JEOL JSM-IT500 InTouchScope™), at an acceleration voltage of 15 kV, after coating the samples with gold.

### 2.4. Continuous degradation of imidacloprid in a flow-cell system

The continuous flow reaction was carried out at room temperature, using the experimental arrangement shown in Fig. S1 (Supplementary Material, SM), which basically consisted of a reservoir containing the pesticide and PMS (1), a peristaltic pump (2), a bubble trap (3), a flow cell (7.7 cm<sup>3</sup>, Sigma-Aldrich) (4), a Xe arc lamp (5) (positioned 15 cm above the flow cell), and a reservoir for the treated solution (6). The cell was irradiated using a solar simulator equipped with a Xe lamp, herein referred to as “solar irradiation” (SI) (Heraeus TQ 150 Xe arc lamp, 18.2 W m<sup>-2</sup>). The same source was combined with a cut-off filter to remove the wavelengths lower than 400 nm, in order to restrict the operation only to the visible radiation region, herein denoted “visible irradiation” (VI) (Heraeus TQ Xe arc lamp with R3114 UV filter, < 3% transmission for light < 400 nm, 16.8 W m<sup>-2</sup>). The emission spectra and light source irradiance were measured with a StellarNet BLUE-Wave spectrometer and are displayed in Fig. S2.

Prior to the degradation assays, the Co<sub>3</sub>O<sub>4</sub> coatings were washed with ultrapure water to remove any excess catalyst. After assembling the catalytic film (5.1 cm<sup>2</sup>) and flow cell (Fig. S1), the solution containing IMD (2.5 mg L<sup>-1</sup>) and PMS (concentrations of 0.1, 0.2, or 0.4 g L<sup>-1</sup>) was pumped through the reactor at a constant flow rate ( $u = 0.10, 0.15, \text{ or } 0.20 \text{ mL min}^{-1}$ ). Three different degradation approaches were studied: (i) catalytic activation of PMS (catalyst + PMS), (ii) heterogeneous photocatalysis (catalyst + irradiation), and (iii) photocatalytic activation of PMS (catalyst + PMS + irradiation). For the purpose of comparison, control assays were performed in the absence of the catalyst, applying the same experimental conditions. The experiments were performed for a maximum of 190 min, established considering the time necessary to reach steady-state, with samples being withdrawn from the reactor at predetermined time intervals. Prior to analysis of the IMD concentration, the samples were filtered using 0.2  $\mu\text{m}$  pore size PVDF membranes and were immediately quenched with excess of methanol. In order to evaluate possible adsorption effects, a solution containing only IMD was fed continuously into the reactor during 1 h, under dark conditions, before starting the oxidation reaction.

Quenching experiments were also carried out to elucidate the main active species involved in the IMD degradation. Accordingly, 1 mM of CH<sub>3</sub>OH, C<sub>4</sub>H<sub>10</sub>O, C<sub>6</sub>H<sub>4</sub>O<sub>2</sub>, or NaN<sub>3</sub> was added to the IMD and PMS solution to scavenge sulfate, hydroxyl, superoxide, and singlet oxygen species, respectively [24].

## 2.5. Analytical procedures

The IMD concentration was measured by high-performance liquid chromatography (HPLC), using an Agilent LC 1260 system fitted with a diode array detector and a C18 ODS HYPERSIL column (5  $\mu\text{m}$ , 150  $\times$  4.6 mm; Thermo Scientific). The analyses were performed at room temperature, employing a mobile phase consisting of 80% ultrapure water and 20%

acetonitrile, at a flow rate of 1.0 mL min<sup>-1</sup>. The detection wavelength was 270 nm. The intermediate compounds formed from the IMD degradation were identified by HPLC-high resolution mass spectrometry (HRMS), using a Bruker maXis II Q-TOF instrument (electrospray ionization mode). A reversed-phase C18 Zorbax-Extend column (5  $\mu\text{m}$ , 150 mm  $\times$  4.6 mm) was used for chromatographic separation, with a mobile phase composed of ultrapure water (79.9%), formic acid (0.1%), and acetonitrile (20%), at a flow rate of 0.8 mL min<sup>-1</sup>. The concentration of total organic carbon (TOC) was determined using a Shimadzu TOC-VCSH system equipped with an ASI-V autosampler. The cobalt concentration was measured in aliquots of the treated solution by inductively coupled plasma optical emission spectroscopy (ICP-OES) (Varian-Agilent 720 with SPS3 injector), in order to determine whether cobalt had been leached from the catalyst during the experiments.

## 3. Results and discussion

### 3.1. Co<sub>3</sub>O<sub>4</sub> characterizations

Fig. 1a shows the X-ray diffractogram of the as-synthesized Co<sub>3</sub>O<sub>4</sub>. The material exhibited eight characteristic diffraction peaks, at  $2\theta$  of 18.94°, 31.17°, 36.72°, 38.42°, 44.66°, 55.46°, 59.15°, and 65.00°, corresponding to the (111), (220), (311), (222), (400), (422), (511), and (440) planes, respectively, of the cubic phase of Co<sub>3</sub>O<sub>4</sub>, according to the ICDS file (01–080–1542, space group Fd3m). Additional phases or impurities were not detected, consistent with the formation of a pure material. The crystallite size of the Co<sub>3</sub>O<sub>4</sub> was 17 nm, according to the Scherrer equation, while the average particle size was 179.5  $\pm$  6.2 nm, determined from DLS measurements. Compared to the value obtained from XRD data, the particle size estimated by DLS was significantly higher, due to agglomeration/aggregation of primary particles in the suspension [25]. The Co<sub>3</sub>O<sub>4</sub> nanoparticles were positively charged, exhibiting a  $\zeta$ -potential of 35.0  $\pm$  0.5 mV at the natural suspension pH (6.86  $\pm$  0.06).

According to the Brunauer-Deming-Deming-Teller (BDDT) classification, the type II N<sub>2</sub> adsorption-desorption isotherm for Co<sub>3</sub>O<sub>4</sub> (Fig. 1b) is commonly ascribed to non-porous, low porosity, or macroporous materials [26]. The BET specific surface area determined from the isotherm was 41.8 m<sup>2</sup> g<sup>-1</sup>. The H3 hysteresis is usually related to mesoporosity, with the observed isotherm loop being characteristic of materials with aggregates of plate-like particles, giving rise to slit-shaped pores [27]. The textural properties of the catalyst are summarized in Table S1, while the cumulative pore volume and pore size distributions are shown in Fig. S3a-b. It was found that the textural properties were governed by mesoporosity (59.3%) and SEM images (top views) of the bare and Co<sub>3</sub>O<sub>4</sub>-coated glass microfiber filters are shown in the Supplementary Material (Figs. S4a and S4b-c, respectively). The Co<sub>3</sub>O<sub>4</sub>

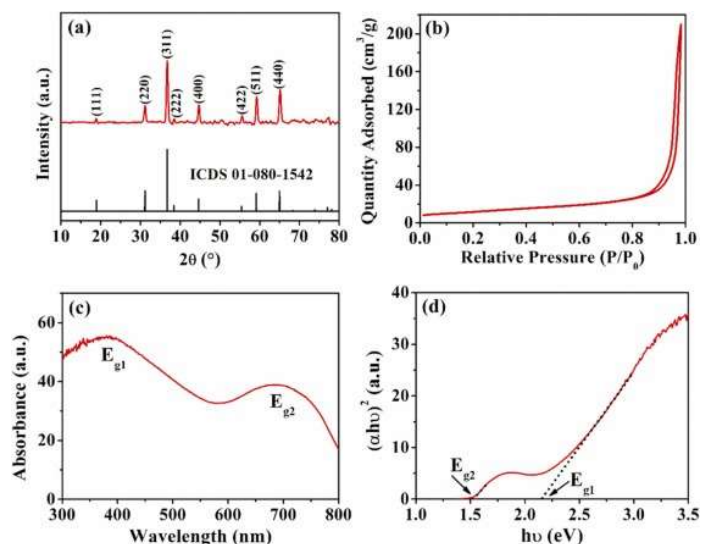


**Figure 1.** XRD pattern, (b) N<sub>2</sub> adsorption-desorption isotherm, (c) UV-Vis absorption spectrum, and (d) Tauc plot for the as-prepared Co<sub>3</sub>O<sub>4</sub> nanoparticles.

macroporosity (40.7%) resulting from particle agglomerates, aggregates, or inter-particle spaces [26]. The Co<sub>3</sub>O<sub>4</sub> presented a trimodal pore distribution in the range of mesopores (Fig. S3b), with pore sizes of around 2.4, 23.6, and 43.6 nm. NPs were successfully deposited as particle aggregates, at the submicron scale, and were evenly distributed over the glass microfiber surface. The presence of larger particles scattered on the surface was also observed.

The optical properties of the Co<sub>3</sub>O<sub>4</sub> were evaluated from the UV-Vis absorption spectra (Fig. 1c). Two absorption bands were observed in the ranges 300–550 nm and 600–800 nm, suggesting that the material could be activated by visible irradiation. The highest energy absorption band ( $E_{g1}$ ) was attributed to charge transfer from O<sup>2-</sup> to Co<sup>2+</sup> (excitation from the optical band gap energy/valence to the conduction band) at the tetrahedral sites of the cubic lattice of Co<sub>3</sub>O<sub>4</sub>. The less energetic absorption band ( $E_{g2}$ ) was ascribed to charge transfer from O<sup>2-</sup> to Co<sup>3+</sup> (Co<sup>3+</sup> level below the conduction band/sub-band located inside the energy gap) in the Co<sub>3</sub>O<sub>4</sub> octahedral sites [28]. The direct band gap energies of Co<sub>3</sub>O<sub>4</sub> were estimated using the Tauc method, by the interception of the tangent lines shown in Fig. 1d with the abscissa of the plot of  $(\alpha h\nu)^2$  against energy ( $h\nu$ ) [28]. The band gap energies  $E_{g1}$  and  $E_{g2}$  were estimated as 2.12 eV and 1.56 eV, respectively, in good agreement with values reported in the literature [29].

### 3.2. Continuous degradation of IMD by Co<sub>3</sub>O<sub>4</sub> in the presence of PMS and solar irradiation

The photochemical performance of the Co<sub>3</sub>O<sub>4</sub> in the continuous-flow system, determined from the IMD degradation experiments, was expressed in terms of the normalized IMD concentration ( $C/C_0$ ) according to reaction time, as shown in Fig. 2 for different reaction conditions. In this figure, the negative values on the abscissa correspond to the time (1 h) during which the

catalyst was in contact with the IMD solution in the absence of PMS and irradiation, in order to identify possible adsorption effects. In this case, the pesticide uptake was less than 5%, demonstrating the low adsorption capacity of Co<sub>3</sub>O<sub>4</sub>, which could be attributed to electrostatic repulsion, since both the Co<sub>3</sub>O<sub>4</sub> surface (positive  $\zeta$ ) and the IMD molecules ( $pK_a = 11.12$  [9]) were positively charged at the working pH. After allowing 60 min for adsorption, the IMD degradation process was started by providing PMS or/and light. As shown in Fig. 2, the oxidation of IMD using PMS alone, photolysis, or photocatalysis was negligible from a practical point of view. In the case of the photocatalysis using Co<sub>3</sub>O<sub>4</sub>, despite the optical properties shown in Fig. 1c, in the absence of PMS the photocatalytic activity was probably hindered by the fast recombination rate of the photogenerated electrons and holes [30] and the improper band edge positions. According to the Butler and Ginley relationship, the valence band (VB) and conduction band (CB) edge potentials of semiconductors at the point of zero charge can be calculated by (1), (2) [31, 32]:

$$E_{CB} = E^o - X - 0.5 E_g \quad (1)$$

$$E_{VB} = E_{CB} + E_g \quad (2)$$

where,  $E_{CB}$  and  $E_{VB}$  are CB and VB edge potentials;  $E^o$  is the energy of free electrons on the hydrogen scale ( $\sim 4.5$  eV);  $X$  is the absolute electronegativity of the semiconductor ( $\sim 5.903$  for Co<sub>3</sub>O<sub>4</sub>); and  $E_g$  is the band gap energy of the semiconductor. Based on these equations, the CB and VB edge potentials values of Co<sub>3</sub>O<sub>4</sub> were then determined to be 0.34 eV and 2.46 eV, respectively, which are in line with those reported by Long et al. [32]. As can be seen, the CB potential of Co<sub>3</sub>O<sub>4</sub> (0.34 eV vs NHE) is more positive than that of O<sub>2</sub>/O<sub>2</sub><sup>-</sup> (-0.33 eV vs NHE), indicating that the photogenerated electrons in the Co<sub>3</sub>O<sub>4</sub> conduction band cannot reduce dissolve oxygen into O<sub>2</sub><sup>-</sup>. Analogously, the VB potential of Co<sub>3</sub>O<sub>4</sub> (2.46 eV vs NHE) is more negative than that of H<sub>2</sub>O/HO<sup>•</sup> (2.72 eV vs NHE), suggesting that photogenerated holes in the Co<sub>3</sub>O<sub>4</sub> valence band cannot oxidize H<sub>2</sub>O into HO<sup>•</sup> [33]. Conversely, there were significant effects of the synergies provided by solar irradiation + PMS and Co<sub>3</sub>O<sub>4</sub> + PMS in the dark, with around 50% and 70% removal, respectively, reached after the transient time. In the first case, PMS could be activated by the UV component of the solar radiation, with the production of active species [34]. In the second case, PMS could be activated by Co<sup>2+</sup> and Co<sup>3+</sup> species in the Co<sub>3</sub>O<sub>4</sub> catalyst structure [23, 35]. Interestingly, when the catalyst, PMS, and solar irradiation were combined, the IMD degradation increased further to 99%, evidencing the roles of different mechanisms contributing to the degradation process. Under this condition, 46% reduction of TOC was achieved at steady-state, indicating the formation of intermediate products. It should be noted that for all the experimental conditions,

the average concentration of cobalt ions released into the solution was not higher than  $33.3 \mu\text{g L}^{-1}$ , which is far below the value allowed by the US EPA for drinking water ( $100 \mu\text{g L}^{-1}$ ).

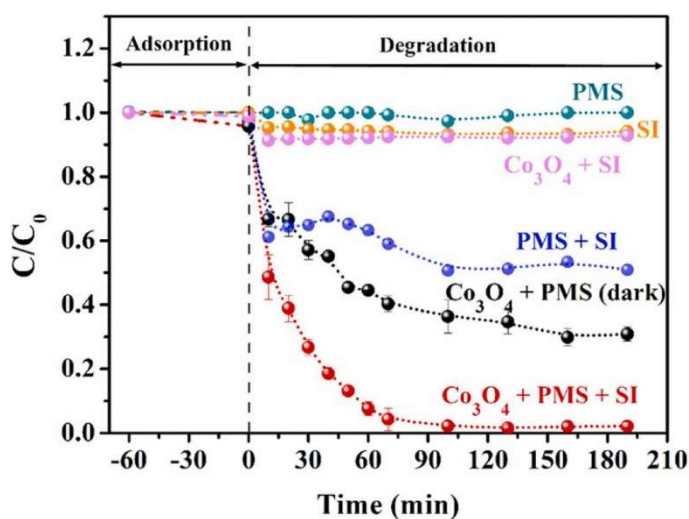
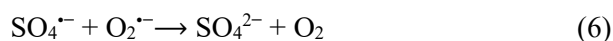
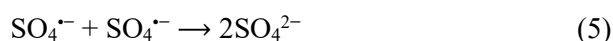
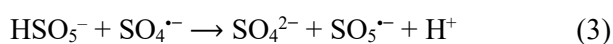


**Figure 2.** IMD degradation curves under different reaction conditions: ● PMS only; ■ photolysis; ◆ photocatalysis (in the absence of PMS); ● PMS and SI; ●  $\text{Co}_3\text{O}_4$  and PMS in the dark; ●  $\text{Co}_3\text{O}_4$  and PMS under SI. Experimental conditions:  $2.5 \text{ mg}_{\text{IMD}} \text{ L}^{-1}$ ;  $0.4 \text{ mg}_{\text{catalyst}} \text{ cm}^{-2}$ ;  $0.2 \text{ g}_{\text{PMS}} \text{ L}^{-1}$ ;  $u = 0.1 \text{ mL min}^{-1}$ .

### 3.3. Influence of operational parameters

Aiming to optimize the PMS-driven and photochemical effects, and to understand the performance of IMD degradation by  $\text{Co}_3\text{O}_4$ , the effects of PMS concentration, flow rate, and type of irradiation were investigated. Fig. 3a-c shows the IMD degradation using different PMS concentrations, in the dark and under solar irradiation. In the absence of light, there was a gradual increase of the IMD removal efficiency as the PMS concentration was increased from  $0.1$  to  $0.4 \text{ g L}^{-1}$ , due to the greater quantity of radicals produced. However, under solar irradiation, the removal efficiency remained almost constant (60%) when the PMS concentration was increased from  $0.2$  to  $0.4 \text{ g L}^{-1}$ . This suggested that an excess of PMS could scavenge sulfate radicals (Eq. 3) [36] or generate reactive species in such concentrations that they scavenged each other, before oxidizing the target pollutant ((4), (5), (6)) [22], consequently inhibiting further IMD degradation. In summary, the synergy achieved by integrating  $\text{Co}_3\text{O}_4$ , PMS, and solar irradiation (Fig. 1b, solar irradiation) allowed the same removal efficiency observed in the absence of light (Fig. 1c, dark), but requiring half of the PMS content, thereby resulting in a more cost-effective and environmentally friendly process. Regarding the effect of flow rate (Fig. 3d-f), higher conversion of IMD was achieved at a low flow rate ( $0.1 \text{ mL min}^{-1}$ ), due to the longer contact and residence time ( $t = 77 \text{ min}$ ) of the fluid in the photoreactor.



The previous results enabled establishment of the experimental conditions for further optimization of the process. In addition, in order to understand the effect of the type of irradiation on IMD degradation, an assay employing visible irradiation was carried out and the results were compared with those obtained under dark and solar irradiation conditions (Fig. 4). Similar performances were observed for the processes in the dark and under visible irradiation, while significant improvement was achieved by exposure to solar irradiation. These results can be understood considering the band gap values of  $2.12 \text{ eV}$  ( $E_{g1}$ ) and  $1.56 \text{ eV}$  ( $E_{g2}$ ), corresponding to  $585 \text{ nm}$  and  $794 \text{ nm}$ , respectively, both present in the visible and solar radiation spectra (Fig. S2a-b). Considering that these wavelengths could photoactivate  $\text{Co}_3\text{O}_4$ , improvements in IMD degradation would be expected, due to the PMS photocatalytic activation mechanism. Therefore, absence of further IMD degradation using the  $\text{Co}_3\text{O}_4/\text{PMS}/\text{VI}$  system indicated that the photocatalytic activation of PMS, involving conduction band electron transfer, did not play a significant role, under the experimental conditions used in this work. In contrast, the positive effects of the  $\text{Co}_3\text{O}_4 + \text{PMS}$  and  $\text{PMS} + \text{SI}$  combinations were clearly evident (Fig. 2d-e). This suggested that the improved degradation efficiency of the  $\text{Co}_3\text{O}_4/\text{PMS}/\text{SI}$  system was mainly due to the activation of PMS by (i)  $\text{Co}^{2+}$  and  $\text{Co}^{3+}$  species in the  $\text{Co}_3\text{O}_4$  catalyst structure, along with the UV component of solar radiation, either (ii) in the homogeneous phase or (iii) following the electrostatic adsorption of PMS onto  $\text{Co}_3\text{O}_4$ . In the third case, the adsorption of negatively charged PMS anions on positively charged  $\text{Co}_3\text{O}_4$  nanoparticles could weaken the bonds of PMS, facilitating and enhancing then its activation by UV irradiation. Liu et al. [37] and Mian and Liun [38] also reported the electrostatic adsorption of PMS by other catalysts.

### 3.4. Mechanism of IMD degradation by $\text{Co}_3\text{O}_4/\text{PMS}/\text{solar irradiation}$

In order to identify the main active species and propose the reaction mechanism for IMD degradation in the  $\text{Co}_3\text{O}_4/\text{PMS}/\text{SI}$  system, quenching experiments were performed using methanol, tert-butyl alcohol, p-benzoquinone, and sodium azide as scavengers. MeOH is a trapping agent for the species  $\text{HO}^{\cdot}$  ( $k = 9.7 \times 10^8 \text{ M}^{-1} \text{ s}^{-1}$ ) and  $\text{SO}_4^{\cdot-}$  ( $k = 2.5 \times 10^7 \text{ M}^{-1} \text{ s}^{-1}$ ) [35, 39, 40], while TBA is selective for  $\text{HO}^{\cdot}$  ( $k = 3.8\text{--}7.6 \times 10^8 \text{ M}^{-1} \text{ s}^{-1}$ ) rather than  $\text{SO}_4^{\cdot-}$  ( $k = 4.0\text{--}9.5 \times 10^5 \text{ M}^{-1} \text{ s}^{-1}$ ) [17, 35]. p-BQ is usually used to capture  $\text{O}_2^{\cdot-}$  [24, 35] and  $\text{NaN}_3$  has a quenching effect on  $^1\text{O}_2$  [24], [37]. As shown in Fig. 5, the addition of TBA had a negligible effect on IMD degradation, in comparison to the blank control, suggesting the minor role of hydroxyl species.

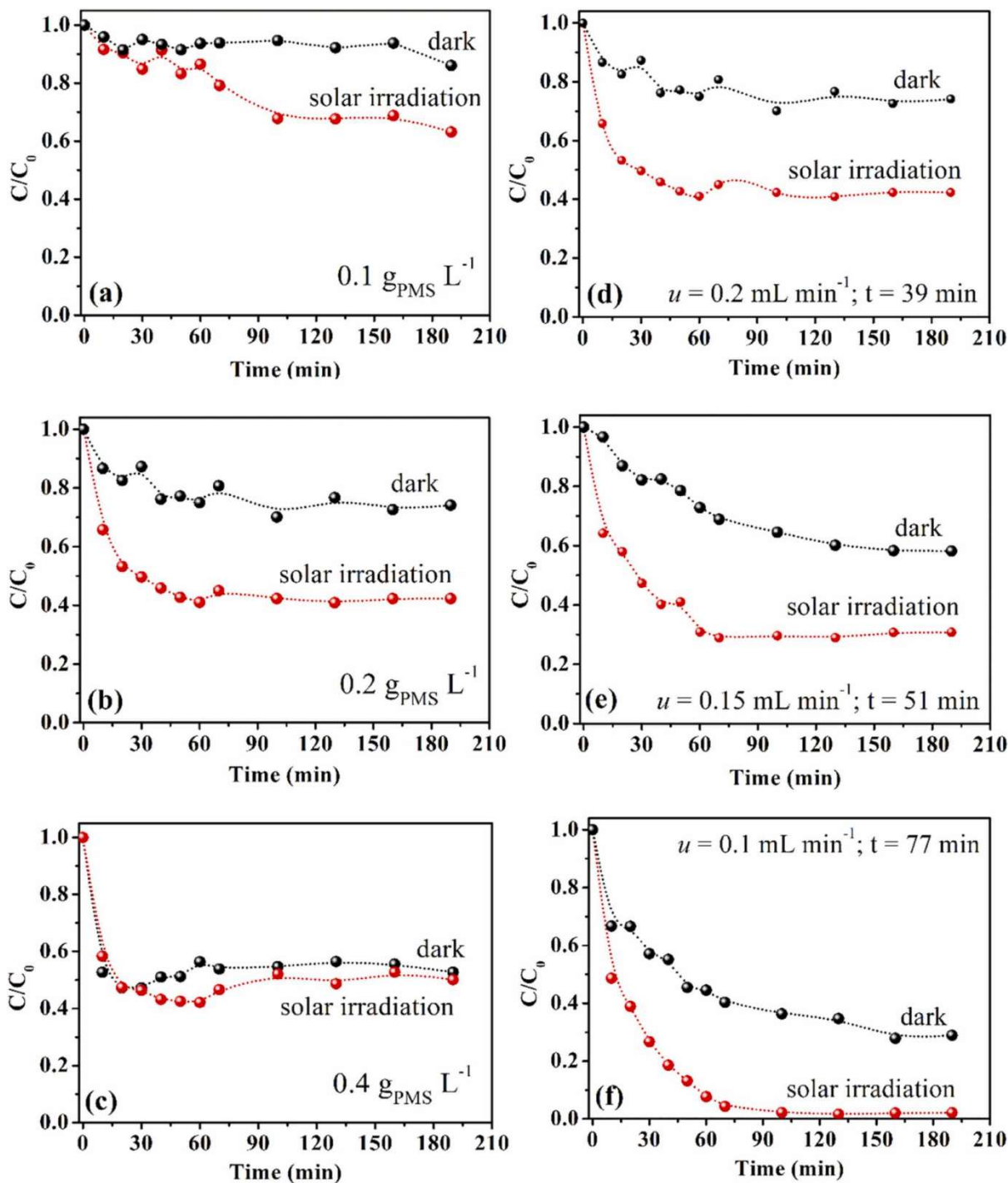


**Figure 3.** Effects of (a-c) PMS concentration, with a flow rate of  $0.2 \text{ mL min}^{-1}$ , and (d-f) flow rate, with PMS concentration of  $0.2 \text{ g}_{\text{PMS}} \text{ L}^{-1}$ , on IMD degradation in the dark and under solar irradiation. Experimental conditions:  $2.5 \text{ mg}_{\text{IMD}} \text{ L}^{-1}$ ;  $0.4 \text{ mg}_{\text{catalyst}} \text{ cm}^{-2}$ .

Conversely, methanol addition led to significant inhibition, while dosing with p-BQ and  $\text{NaN}_3$  resulted in complete inhibition. Considering the lower oxidation potential of  $\text{O}_2^{\cdot-}$ , compared to  $^1\text{O}_2$  [35], [40], the latter was probably the main species responsible for IMD degradation. In summary, it was demonstrated that  $\text{SO}_4^{\cdot-}$ ,  $\text{O}_2^{\cdot-}$ , and  $^1\text{O}_2$  were the reactive species associated with IMD removal in the  $\text{Co}_3\text{O}_4/\text{PMS}/\text{SI}$  system. It is worth mentioning that the development of processes dominated by singlet oxygen, which is not usual in other AOPs, has been gaining attention for water

treatment purposes, since recent studies have reported that  $^1\text{O}_2$ , rather than  $\text{HO}^{\cdot}$  and  $\text{SO}_4^{\cdot-}$ , is the main reactive species for degradation of organic pollutants [17], [35], [37], as well as for disinfection to eliminate microorganisms [40], [41].

Based on the results described above, a possible mechanism for IMD photodegradation was proposed. According to (7), (8),  $\text{SO}_4^{\cdot-}$  and  $\text{HO}^{\cdot}$  radicals could be generated by means of the photoactivation of PMS by the UV component of solar radiation, either through

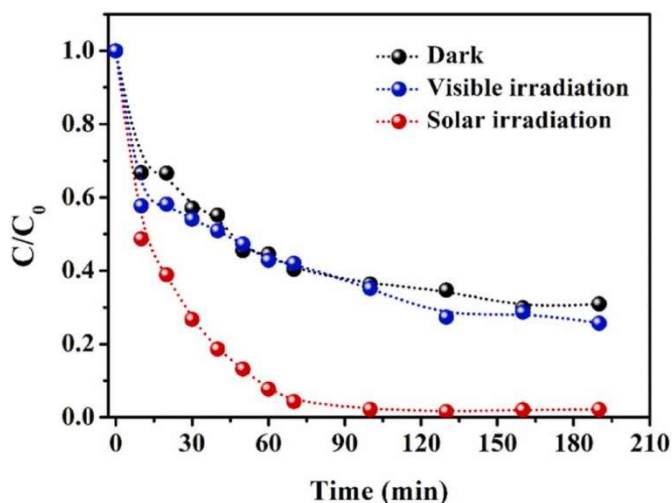


**Figure 4.** Effect of different irradiation types on IMD degradation. Experimental conditions:  $2.5 \text{ mg}_{\text{IMD}} \text{ L}^{-1}$ ;  $0.4 \text{ mg}_{\text{catalyst}} \text{ cm}^{-2}$ ;  $u = 0.1 \text{ mL min}^{-1}$ .

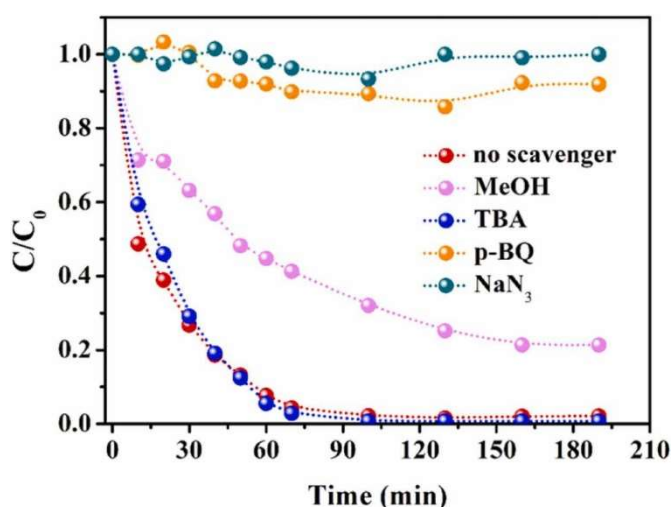
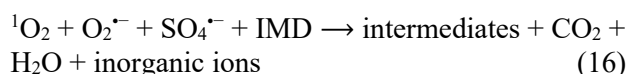
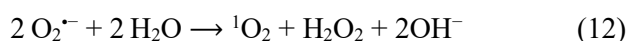
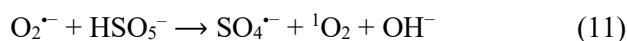
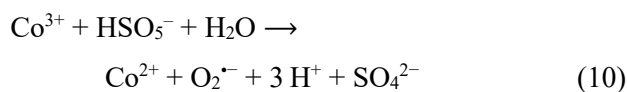
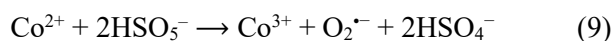
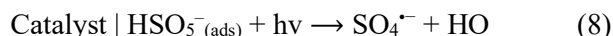


**Figure 5.** IMD degradation using the  $\text{Co}_3\text{O}_4/\text{PMS}/\text{SI}$  approach in the presence of different radical scavenger species. Experimental conditions:  $2.5 \text{ mg}_{\text{IMD}} \text{ L}^{-1}$ ;  $0.4 \text{ mg}_{\text{catalyst}} \text{ cm}^{-2}$ ;  $0.2 \text{ g}_{\text{PMS}} \text{ L}^{-1}$ ;  $u = 0.1 \text{ mL min}^{-1}$ . Scavenger concentration:  $1 \text{ mM}$ ; solar irradiation:  $18.2 \text{ W m}^{-2}$ .

direct photolysis of PMS in the aqueous phase [22] or following its electrostatic adsorption onto  $\text{Co}_3\text{O}_4$  surface, respectively. Due to the positive surface charge of the catalyst,  $\text{Co}_3\text{O}_4$  might chemically adsorb  $\text{HSO}_5^-$  and weaken its bonds, facilitating then its photoactivation. Simultaneously,  $\text{Co}^{2+}$  and  $\text{Co}^{3+}$  could react chemically with PMS in a cyclic  $\text{Co}^{3+}/\text{Co}^{2+}$  redox process, producing  $\text{O}_2^{\cdot-}$  ((9), (10)) [35], [42]. Next,  $\text{O}_2^{\cdot-}$  could give rise to  $^1\text{O}_2$  upon oxidation (Eq. 11) or recombination (Eq. 12) [17], [24]. Additionally, the produced  $\text{HO}^{\cdot}$  could further accelerate the PMS decomposition and generate  $\text{SO}_5^{\cdot-}$  radicals (Eq. 13) [43], [44]. Then, the  $\text{SO}_5^{\cdot-}$  radicals could react with each other to produce  $\text{SO}_4^{\cdot-}$  via Eq. 14 [43], [44], and part of the  $\text{SO}_4^{\cdot-}$  could be converted into  $^1\text{O}_2$ , according to Eq. 15 [24]. Finally,  $\text{SO}_4^{\cdot-}$ ,  $\text{O}_2^{\cdot-}$ , and  $^1\text{O}_2$  could oxidize the IMD, converting it to intermediate compounds or eventually mineralizing it to carbon

dioxide, water, and inorganic ions such as  $\text{NO}_2^-$  and  $\text{Cl}^-$  (Eq. 16).



### 3.5. Pathway of IMD degradation by $\text{Co}_3\text{O}_4/\text{PMS}/\text{solar}$ irradiation

In addition to the IMD reaction mechanism, a degradation pathway was proposed from identification of the intermediate compounds found in the HRMS-HPLC analysis. Table 1 shows the main identified products, suggesting three possible degradation routes (R1, R2, and R3), displayed in Fig. 6. In route R1, the amidine nitrogen site of IMD can be attacked by the  $^1\text{O}_2$ , yielding a nitrogen-centered radical cation, which upon the elimination of one hydrogen atom from the  $\text{CH}_2$  units of the 5-member ring leads the formation of an  $\alpha$ -aminoalkyl radical. Next, the  $\alpha$ -aminoalkyl radical may quickly react with dissolved oxygen (DO) to produce the hydroxylated and carbonylated intermediates, I1 and I2 [45]. Further hydroxylation of I1 yields the product I3 [10]. Subsequently, I3 can be converted to I4 by loss of the nitro group ( $-\text{NO}_2$ ). In the next steps, I4 can be further converted to I5 and then to 6-chloronicotinic acid (I6) or be directly converted to I6 [46]. Concurrently, in route R2, a similar reaction path as that observed for R1 takes place. However, the H-abstraction occurs in methylene bridge and the  $\alpha$ -aminoalkyl radical reacts directly with DO and water to form I6 [45]. Subsequent degradation of I6 may eventually lead the cleavage of its aromatic ring yielding the formation of several short-linear molecules, including oxamic and oxalic acid, as a preceding step to complete mineralization to  $\text{CO}_2$ ,  $\text{H}_2\text{O}$  and inorganic salts [47], [48]. It is also worth noting that two high molecular weight products were detected (I7 and I8), which were probably oligomers of undetected dechlorinated fragments generated during the degradation process (route 3). Among the formed by-products, the intermediates I1, I3 [49] and I4 [50] are considered to be less toxic for *Daphnia* and *Green Algae* than IMD by the ECOSAR analysis. In contrast, the predicted toxicity of 6-chloronicotinic for *Daphnia* and fish was found to be

higher than that of the parent compound [51]. Therefore, future works need to conduct toxicity assessments in order to ensure a better comprehension of the impact of intermediates in the Co<sub>3</sub>O<sub>4</sub>/PMS/SI process.

**Table 1.** IMD degradation intermediates in the Co<sub>3</sub>O<sub>4</sub>/PMS/SI process, detected by HRMS-HPLC.

Compound	Formula	Experimental mass (m/z)	Calculated mass (m/z)	Error (ppm)
IMD	C <sub>9</sub> H <sub>10</sub> ClN <sub>5</sub> O <sub>2</sub>	255.0518	255.0517	0.1
I1	C <sub>9</sub> H <sub>10</sub> ClN <sub>5</sub> O <sub>3</sub>	271.0467	271.0467	0.0
I2	C <sub>9</sub> H <sub>8</sub> ClN <sub>5</sub> O <sub>3</sub>	269.0310	269.0312	-0.6
I3	C <sub>9</sub> H <sub>10</sub> ClN <sub>5</sub> O <sub>4</sub>	287.0416	287.0419	-0.8
I4	C <sub>9</sub> H <sub>11</sub> ClN <sub>4</sub> O <sub>2</sub>	242.0565	242.0566	-0.1
I5	C <sub>7</sub> H <sub>9</sub> ClN <sub>4</sub>	184.0511	184.0507	1.7
I6	C <sub>6</sub> H <sub>4</sub> ClNO <sub>2</sub>	156.9925	156.9923	1.8
I7	C <sub>24</sub> H <sub>44</sub> N <sub>4</sub> O <sub>4</sub>	452.3357	452.3358	-0.1
I8	C <sub>36</sub> H <sub>66</sub> N <sub>6</sub> O <sub>6</sub>	678.5033	678.5039	0.9

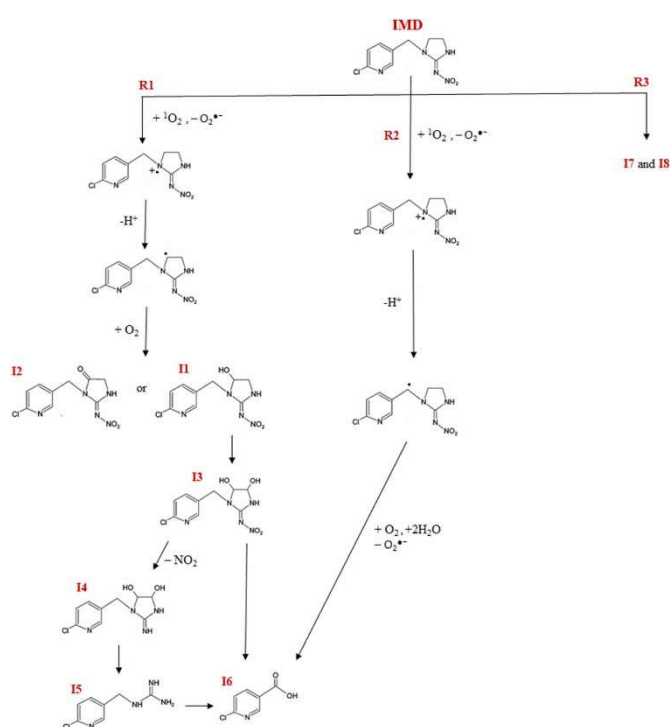


**Figure 1.** IMD degradation pathway in the Co<sub>3</sub>O<sub>4</sub>/PMS/SI process.

#### 4. Conclusions

Cubic-phase Co<sub>3</sub>O<sub>4</sub> nanoparticles were successfully synthesized by a simple precipitation/calcination method. These nanoparticles were then immobilized on glass microfiber substrates, by vacuum filtration deposition from stable suspensions of positively charged aggregates. The photochemical performance of the as-prepared Co<sub>3</sub>O<sub>4</sub> coatings for IMD degradation by PMS was investigated using a continuous flow-cell reactor, with detailed evaluation of the effects of PMS concentration, flow rate, and type of irradiation. Adsorption, photolysis, photocatalysis, and the presence of only PMS were found to lead to negligible IMD removal. The combination of PMS with solar irradiation or with Co<sub>3</sub>O<sub>4</sub> led to IMD removals of

~50% and ~70%, respectively. The highest performance (99% removal) was achieved using the Co<sub>3</sub>O<sub>4</sub>/PMS/solar irradiation combination, which could be attributed to the synergistic activation of PMS by the UV component of the solar radiation and the Co<sub>3</sub>O<sub>4</sub> catalyst. The optimal operational conditions were found to be a PMS concentration of 0.2 g L<sup>-1</sup>, a flow rate of 0.1 mL min<sup>-1</sup> (residence time 77 min), and full-spectrum (solar) irradiation. Under the experimental conditions used in this work, the photogenerated electrons in the Co<sub>3</sub>O<sub>4</sub> did not play a significant role, but the electrostatic interaction of PMS and Co<sub>3</sub>O<sub>4</sub> considerably increased the efficiency of solar irradiation for the activation of PMS. Sulfate and superoxide radicals, as well as singlet oxygen, were the main active species associated with IMD removal. Eight intermediate degradation products were identified. Finally, it could be concluded that the Co<sub>3</sub>O<sub>4</sub>/PMS/solar irradiation technique is capable of providing efficient degradation of IMD in continuous systems, enabling reduction of the PMS concentration and making the process more sustainable.

#### Acknowledgements

The authors are grateful for financial support provided by the National Council of Technological and Scientific Development, Brazil (CNPq, grant number 142087/2019-0), and MCIN/AEI/10.13039/501100011033, RTI2018-094958-B-I00. R. R. Maciel-Silva thanks Coordenação de Aperfeiçoamento de Pessoal de Nível Superior, Brazil, for a sandwich doctorate scholarship (CAPES, grant number 88887.571964/2020-00).

#### References

- [1] M.M. Sablas, M.D.G. de Luna, S. García-Segura, C.W. Chen, C.F. Chen, C. Di Dong, Percarbonate mediated advanced oxidation completely degrades recalcitrant pesticide imidacloprid: Role of reactive oxygen species and transformation products, *Sep. Purif. Technol.* 250 (2020), 117269, <https://doi.org/10.1016/j.seppur.2020.117269>.
- [2] C.M. Batikian, A. Lu, K. Watanabe, J. Pitt, R.M. Gersberg, Temporal pattern in levels of the neonicotinoid insecticide, imidacloprid, in an urban stream, *Chemosphere* 223 (2019) 83–90, <https://doi.org/10.1016/j.chemosphere.2019.01.165>.
- [3] L.P. Belzunces, J.M. Bonmatin, M. Chagnon, C. Downs, Systemic insecticides (neonicotinoids and fipronil): trends, uses, mode of action and metabolites, *Environ. Sci. Pollut. Res. Int.* 22 (2015) 5–34, <https://doi.org/10.1007/s11356-014-3470-y>.
- [4] D.A. Thompson, H.J. Lehmler, D.W. Kolpin, M.L. Hladik, J.D. Vargo, K.E. Schilling, G.H. Lefevre, T.L. Peebles, M.C. Poch, L.E. Laduca, D.M. Cwiertny, R.W. Field, A critical review on the potential impacts of neonicotinoid insecticide

- use: current knowledge of environmental fate, toxicity, and implications for human health, *Environ. Sci. Process. Impacts* 22 (2020) 1315–1346, <https://doi.org/10.1039/c9em00586b>.
- [5] M. Lamers, M. Anyusheva, N. La, V.V. Nguyen, T. Streck, Pesticide pollution in surface and groundwater by paddy rice cultivation: a case study from Northern Vietnam, *Clean. - Soil, Air, Water* 39 (2011) 356–361, <https://doi.org/10.1002/clen.201000268>.
- [6] C.A. Morrissey, P. Mineau, J.H. Devries, F. Sanchez-Bayo, M. Liess, M.C. Cavallaro, K. Liber, Neonicotinoid contamination of global surface waters and associated risk to aquatic invertebrates: a review, *Environ. Int.* 74 (2015) 291–303, <https://doi.org/10.1016/j.envint.2014.10.024>.
- [7] C.M. Rocha, A.M. Lastre-Acosta, M.P.S. Parizi, A.C.S.C. Teixeira, Environmental photochemical fate of pesticides ametryn and imidacloprid in surface water (Parapanema River, Sao Paulo, Brazil), *Environ. Sci. Pollut. Res.* 29 (2022) 42290–42304, <https://doi.org/10.1007/s11356-021-17991-5>.
- [8] J.C. Anderson, C. Dubetz, V.P. Palace, Neonicotinoids in the Canadian aquatic environment: a literature review on current use products with a focus on fate, exposure, and biological effects, *Sci. Total Environ.* 505 (2015) 409–422, <https://doi.org/10.1016/j.scitotenv.2014.09.090>.
- [9] Y. Ma, L. Wu, P. Li, L. Yang, L. He, S. Chen, Y. Yang, F. Gao, X. Qi, Z. Zhang, A novel, efficient and sustainable magnetic sludge biochar modified by graphene oxide for environmental concentration imidacloprid removal, *J. Hazard. Mater.* 407 (2021), <https://doi.org/10.1016/j.jhazmat.2020.124777>.
- [10] J. Tan, Z. Li, J. Li, Y. Meng, X. Yao, Y. Wang, Y. Lu, T. Zhang, Visible-light-assisted peroxymonosulfate activation by metal-free bifunctional oxygen-doped graphitic carbon nitride for enhanced degradation of imidacloprid: Role of non-photochemical and photocatalytic activation pathway, *J. Hazard. Mater.* 423 (2022), 127048, <https://doi.org/10.1016/j.jhazmat.2021.127048>.
- [11] M. Kanwal, S.R. Tariq, G.A. Chotana, Photocatalytic degradation of imidacloprid by Ag-ZnO composite, *Environ. Sci. Pollut. Res.* 25 (2018) 27307–27320, <https://doi.org/10.1007/s11356-018-2693-8>.
- [12] M. Naghizadeh, M.A. Taher, A.M. Tamaddon, Facile synthesis and characterization of magnetic nanocomposite ZnO/CoFe<sub>2</sub>O<sub>4</sub> hetero-structure for rapid photocatalytic degradation of imidacloprid, *Heliyon* 5 (2019), e02870, <https://doi.org/10.1016/j.heliyon.2019.e02870>.
- [13] J. Li, W. Huang, L. Yang, G. Gou, C. Zhou, L. Li, N. Li, C. Liu, B. Lai, Novel Ag<sub>3</sub>PO<sub>4</sub> modified tubular carbon nitride with visible-light-driven peroxymonosulfate activation: a wide pH tolerance and reaction mechanism, *Chem. Eng. J.* 432 (2022), 133588, <https://doi.org/10.1016/j.cej.2021.133588>.
- [14] J. Li, L. Yang, B. Lai, C. Liu, Y. He, G. Yao, N. Li, Recent progress on heterogeneous Fe-based materials induced persulfate activation for organics removal, *Chem. Eng. J.* 414 (2021), 128674, <https://doi.org/10.1016/j.cej.2021.128674>.
- [15] J. Li, G. Gou, H. Zhao, C. Liu, N. Li, L. Li, B. Tan, B. Lai, Efficient peroxymonosulfate activation by CoFe<sub>2</sub>O<sub>4</sub>-CeO<sub>2</sub> composite: performance and catalytic mechanism, *Chem. Eng. J.* 435 (2022), 134840, <https://doi.org/10.1016/j.cej.2022.134840>.
- [16] F. Ghanbari, M. Moradi, Application of peroxymonosulfate and its activation methods for degradation of environmental organic pollutants: review, *Chem. Eng. J.* 310 (2017) 41–62, <https://doi.org/10.1016/j.cej.2016.10.064>.
- [17] J. Hu, X. Zeng, G. Wang, B. Qian, Y. Liu, X. Hu, B. He, L. Zhang, X. Zhang, Modulating mesoporous Co<sub>3</sub>O<sub>4</sub> hollow nanospheres with oxygen vacancies for highly efficient peroxymonosulfate activation, *Chem. Eng. J.* 400 (2020), 125869, <https://doi.org/10.1016/j.cej.2020.125869>.
- [18] G.P. Anipsitakis, D.D. Dionysiou, Radical generation by the interaction of transition metals with common oxidants, *Environ. Sci. Technol.* 38 (2004) 3705–3712, <https://doi.org/10.1021/es035121o>.
- [19] P.R. Shukla, S. Wang, H. Sun, H.M. Ang, M. Tadé, Activated carbon supported cobalt catalysts for advanced oxidation of organic contaminants in aqueous solution, *Appl. Catal. B Environ.* 100 (2010) 529–534, <https://doi.org/10.1016/j.apcatb.2010.09.006>.
- [20] G.P. Anipsitakis, E. Stathatos, D.D. Dionysiou, Heterogeneous activation of Oxone using Co<sub>3</sub>O<sub>4</sub>, *J. Phys. Chem. B* 109 (2005) 13052–13055, <https://doi.org/10.1021/jp052166y>.
- [21] X. Chen, J. Chen, X. Qiao, D. Wang, X. Cai, Performance of nano-Co<sub>3</sub>O<sub>4</sub>/peroxymonosulfate system: Kinetics and mechanism study using Acid Orange 7 as a model compound, *Appl. Catal. B Environ.* 80 (2008) 116–121, <https://doi.org/10.1016/j.apcatb.2007.11.009>.
- [22] Y. Wang, L. Zhou, X. Duan, H. Sun, E.L. Tin, W. Jin, S. Wang, Photochemical degradation of phenol solutions on Co<sub>3</sub>O<sub>4</sub> nanorods with sulfate radicals, *Catal. Today* 258 (2015) 576–584, <https://doi.org/10.1016/j.cattod.2014.12.020>.
- [23] C.H. Shen, X.J. Wen, Z.H. Fei, Z.T. Liu, Q.M. Mu, Visible-light-driven activation of peroxymonosulfate for accelerating ciprofloxacin degradation using CeO<sub>2</sub>/Co<sub>3</sub>O<sub>4</sub> p-n heterojunction photocatalysts, *Chem. Eng. J.* 391

- (2020), 123612,  
<https://doi.org/10.1016/j.cej.2019.123612>.
- [24] T. Ni, Z. Yang, H. Zhang, L. Zhou, W. Guo, L. Pan, Z. Yang, K. Chang, C. Ge, D. Liu, Peroxymonosulfate activation by  $\text{Co}_3\text{O}_4/\text{SnO}_2$  for efficient degradation of ofloxacin under visible light, *J. Colloid Interface Sci.* 615 (2022) 650–662, <https://doi.org/10.1016/j.jcis.2022.02.024>.
- [25] L. Valenzuela, A. Iglesias, M. Faraldos, A. Bahamonde, R. Rosal, Antimicrobial surfaces with self-cleaning properties functionalized by photocatalytic ZnO electrosprayed coatings, *J. Hazard. Mater.* 369 (2019) 665–673, <https://doi.org/10.1016/j.jhazmat.2019.02.073>.
- [26] C. Adán, A. Martínez-Arias, M. Fernández-García, A. Bahamonde, Photocatalytic degradation of ethidium bromide over titania in aqueous solutions, *Appl. Catal. B Environ.* 76 (2007) 395–402, <https://doi.org/10.1016/j.apcatb.2007.06.013>.
- [27] S.-H. Chai, H.-P. Wang, Y. Liang, B.-Q. Xu, Sustainable production of acrolein: Gas-phase dehydration of glycerol over  $\text{Nb}_2\text{O}_5$  catalyst, *J. Catal.* 250 (2007) 342–349, <https://doi.org/10.1016/j.jcat.2007.06.016>.
- [28] M. Aadil, S. Zulfiqar, M.F. Warsi, P.O. Agboola, I. Shakir, M. Shahid, N.F. Al-Khalli, Mesoporous and macroporous Ag-doped  $\text{Co}_3\text{O}_4$  nanosheets and their superior photo-catalytic properties under solar light irradiation, *Ceram. Int.* 47 (2021) 9806–9817, <https://doi.org/10.1016/j.ceramint.2020.12.121>.
- [29] A. Gulino, P. Dapporto, P. Rossi, I. Fragala, A novel self-generating liquid MOCVD precursor for  $\text{Co}_3\text{O}_4$  thin films, *Mater* 15 (2003) 3748–3752, <https://doi.org/10.1021/cm034305z>.
- [30] J. Liu, D. Wang, M. Wang, D. Kong, Y. Zhang, J.F. Chen, L. Dai, Uniform two-dimensional  $\text{Co}_3\text{O}_4$  porous sheets: facile synthesis and enhanced photocatalytic performance, *Chem. Eng. Technol.* 39 (2016) 891–898, <https://doi.org/10.1002/ceat.201500542>.
- [31] P. Praus, On electronegativity of graphitic carbon nitride, *Carbon N. Y* 172 (2021) 729–732, <https://doi.org/10.1016/j.carbon.2020.10.074>.
- [32] M. Long, W. Cai, J. Cai, B. Zhou, X. Chai, Y. Wu, Efficient photocatalytic degradation of phenol over  $\text{Co}_3\text{O}_4/\text{BiVO}_4$  composite under visible light irradiation, *J. Phys. Chem. B* 110 (2006) 20211–20216, <https://doi.org/10.1021/jp063441z>.
- [33] A.C. Nogueira, L.E. Gomes, J.A.P. Ferencz, J.E.F.S. Rodrigues, R.V. Gonçalves, H. Wender, Improved visible light photoactivity of  $\text{CuBi}_2\text{O}_4/\text{CuO}$  heterojunctions for photodegradation of methylene blue and metronidazole, *J. Phys. Chem. C* 123 (2019) 25680–25690, <https://doi.org/10.1021/acs.jpcc.9b06907>.
- [34] Q. Wang, P. Rao, G. Li, L. Dong, X. Zhang, Y. Shao, N. Gao, W. Chu, B. Xu, N. An, J. Deng, Degradation of imidacloprid by UV-activated persulfate and peroxymonosulfate processes: kinetics, impact of key factors and degradation pathway, *Ecotoxicol. Environ. Saf.* 187 (2020), 109779, <https://doi.org/10.1016/j.ecoenv.2019.109779>.
- [35] Z. Liu, X. Tanga, G. Huang, X. Luoc, D. Hed, Q. Penga, J. Huang, M. Aoa, K. Liu, Bismuth MOFs based hierarchical  $\text{Co}_3\text{O}_4\text{-Bi}_2\text{O}_3$  composite: an efficient heterogeneous peroxymonosulfate activator for azo dyes degradation, *Sep. Purif. Technol.* 242 (2020), 116825, <https://doi.org/10.1016/j.seppur.2020.116825>.
- [36] H. Zhang, L. chao Nengzi, X. Li, Z. Wang, B. Li, L. Liu, X. Cheng, Construction of  $\text{CuBi}_2\text{O}_4/\text{MnO}_2$  composite as Z-scheme photoactivator of peroxymonosulfate for degradation of antibiotics, *Chem. Eng. J.* 386 (2020), 124011, <https://doi.org/10.1016/j.cej.2020.124011>.
- [37] S. Liu, Z. Zhang, F. Huang, Y. Liu, L. Feng, J. Jiang, L. Zhang, F. Qi, C. Liu, Carbonized polyaniline activated peroxymonosulfate (PMS) for phenol degradation: role of PMS adsorption and singlet oxygen generation, *Appl. Catal. B Environ.* 286 (2021), 119921, <https://doi.org/10.1016/j.apcatb.2021.119921>.
- [38] M.M. Mian, G. Liu, Activation of peroxymonosulfate by chemically modified sludge biochar for the removal of organic pollutants: understanding the role of active sites and mechanism, *Chem. Eng. J.* 392 (2020), 123681, <https://doi.org/10.1016/j.cej.2019.123681>.
- [39] J. Guo, C.H. Shen, J. Sun, X.J. Xu, X.Y. Li, Z.H. Fei, Z.T. Liu, X.J. Wen, Highly efficient activation of peroxymonosulfate by  $\text{Co}_3\text{O}_4/\text{Bi}_2\text{MoO}_6$  p-n heterostructure composites for the degradation of norfloxacin under visible light irradiation, *Sep. Purif. Technol.* 259 (2021), 118109, <https://doi.org/10.1016/j.seppur.2020.118109>.
- [40] Y. Jiang, Z. Wang, J. Huang, F. Yan, Y. Du, C. He, Y. Liu, G. Yao, B. Lai, A singlet oxygen dominated process through photocatalysis of CuS-modified MIL-101(Fe) assisted by peroxymonosulfate for efficient water disinfection, *Chem. Eng. J.* 439 (2022), 135778, <https://doi.org/10.1016/j.cej.2022.135778>.
- [41] D. García-Fresnadillo, Singlet oxygen photosensitizing materials for point-of-use water disinfection with solar reactors, *ChemPhotoChem* 2 (2018) 512–534, <https://doi.org/10.1002/cptc.201800062>.
- [42] J. Fan, H. Qin, S. Jiang, Mn-doped g-C<sub>3</sub>N<sub>4</sub> composite to activate peroxymonosulfate for acetaminophen degradation: the role of

- superoxide anion and singlet oxygen, *Chem. Eng. J.* 359 (2019) 723–732, <https://doi.org/10.1016/j.cej.2018.11.165>.
- [43] Y.H. Guan, J. Ma, X.C. Li, J.Y. Fang, L.W. Chen, Influence of pH on the formation of sulfate and hydroxyl radicals in the UV/Peroxymonosulfate system, *Environ. Sci. Technol.* 45 (2011) 9308–9314, <https://doi.org/10.1021/es2017363>.
- [44] X. Liu, T. Zhang, Y. Zhou, L. Fang, Y. Shao, Degradation of atenolol by UV/peroxymonosulfate: kinetics, effect of operational parameters and mechanism, *Chemosphere* 93 (2013) 2717–2724, <https://doi.org/10.1016/j.chemosphere.2013.08.090>.
- [45] M.L. Dell’Arciprete, L. Santos-Juanes, A. Arques, R.F. Vercher, A.M. Amat, J. P. Furlong, D.O. Martíre, M.C. Gonzalez, Reactivity of neonicotinoid pesticides with singlet oxygen, *Catal. Today* 151 (2010) 137–142, <https://doi.org/10.1016/j.cattod.2010.01.020>.
- [46] T. Roberts, D. Hutson, *Metabolic Pathways of Agrochemicals: Part 2, Insecticides and Fungicides*. The Royal Society of Chemistry, Cornwall, UK, 1999, <https://doi.org/10.1039/9781847551375-00937>.
- [47] D. Mohanta, M. Ahmaruzzaman, Au–SnO<sub>2</sub>–CdS ternary nanoheterojunction composite for enhanced visible light-induced photodegradation of imidacloprid, *Environ. Res.* 201 (2021), 111586, <https://doi.org/10.1016/j.envres.2021.111586>.
- [48] C.F.Z. Lacson, M.D.G. de Luna, C. Dong, S. García-Segura, M.C. Lu, Fluidized-bed Fenton treatment of imidacloprid: optimization and degradation pathway, *Sustain. Environ. Res.* 28 (2018) 309–314, <https://doi.org/10.1016/j.serj.2018.09.001>.
- [49] C. Zhang, F. Li, H. Zhang, R. Wen, X. Yi, Y. Yang, J. He, G.G. Ying, M. Huang, Crucial roles of 3D–MoO<sub>2</sub>–PBC cocatalytic electrodes in the enhanced degradation of imidacloprid in heterogeneous electro–Fenton system: Degradation mechanisms and toxicity attenuation, *J. Hazard. Mater.* 420 (2021), <https://doi.org/10.1016/j.jhazmat.2021.126556>.
- [50] M. Voigt, V. Langerbein, M. Jaeger, In silico ecotoxicity assessment of photoinduced imidacloprid degradation using HPLC–HRMS, QSAR and ecotoxicity equivalents, *Environ. Sci. Eur.* 34 (2022), <https://doi.org/10.1186/s12302-022-00616-0>.
- [51] Q. Kan, K. Lu, S. Dong, D. Shen, Q. Huang, Y. Tong, W. Wu, S. Gao, L. Mao, Transformation and removal of imidacloprid mediated by silver ferrite nanoparticle facilitated peroxymonosulfate activation in water: Reaction rates, products, and pathways, *Environ. Pollut.* 267 (2020), 115438, <https://doi.org/10.1016/j.envpol.2020.115438>.

# Supplementary Material

## Peroxymonosulfate activation by $\text{Co}_3\text{O}_4$ coatings for imidacloprid degradation in a continuous flow-cell reactor under simulated solar irradiation

Roberta R.M. Silva<sup>1,\*</sup>, Laura Valenzuela<sup>2</sup>, Roberto Rosal<sup>2</sup>, Luís A.M. Ruotolo<sup>1</sup>, Francisco G.E. Nogueira<sup>1</sup>, Ana Bahamonde<sup>3</sup>

<sup>1</sup> Department of Chemical Engineering, Federal University of São Carlos, Rod. Washington Luiz, km 235, São Carlos, SP 13565-905, Brazil

<sup>2</sup> Department of Chemical Engineering, University of Alcalá, Alcalá de Henares, Madrid E-28871, Spain

<sup>3</sup> Instituto de Catálisis y Petroleoquímica, ICP-CSIC, Marie Curie 2, 28049 Madrid, Spain

### Contents:

**Table S1.** Summary of the textural properties of the  $\text{Co}_3\text{O}_4$ .

**Fig. S1.** Schematic representation of the experimental arrangement used for IMD degradation: (1) reservoir containing the pesticide and PMS, (2) peristaltic pump, (3) bubble trap, (4) flow cell ( $7.7 \text{ cm}^3$ , Sigma-Aldrich), (5) Xe arc lamp (15 cm above the flow cell), and (6) reservoir for the treated solution.

**Fig. S2.** Emission spectra of the Heraeus TQ 150 Xe arc lamp (a) and the Heraeus TQ Xe arc lamp with R3114 UV filter (b).

**Fig. S3.** Cumulative pore volume (a) and pore size (b) distributions of the as-synthesized  $\text{Co}_3\text{O}_4$  nanoparticles.

**Fig. S4.** Top-view SEM images of the glass microfiber filter substrate (a) and the  $\text{Co}_3\text{O}_4$ -coated substrate fabricated by vacuum filtration (b-c).

**Table S1.** Summary of the textural properties of the  $\text{Co}_3\text{O}_4$ .

Catalyst	$S_{\text{BET}}$ ( $\text{m}^2 \text{ g}^{-1}$ )	$A_{\text{external}}$ ( $\text{m}^2 \text{ g}^{-1}$ )	$A_{\text{micro}}$ ( $\text{m}^2 \text{ g}^{-1}$ )	$V_{\text{micropores}}$ ( $\text{cm}^3 \text{ g}^{-1}$ )	$V_{\text{mesopores}}$ ( $\text{cm}^3 \text{ g}^{-1}$ )	$V_{\text{macropores}}$ ( $\text{cm}^3 \text{ g}^{-1}$ )	$V_{\text{total}}$ ( $\text{cm}^3 \text{ g}^{-1}$ )
$\text{Co}_3\text{O}_4$	41.8	40.4	1.4	-	0.19	0.13	0.32

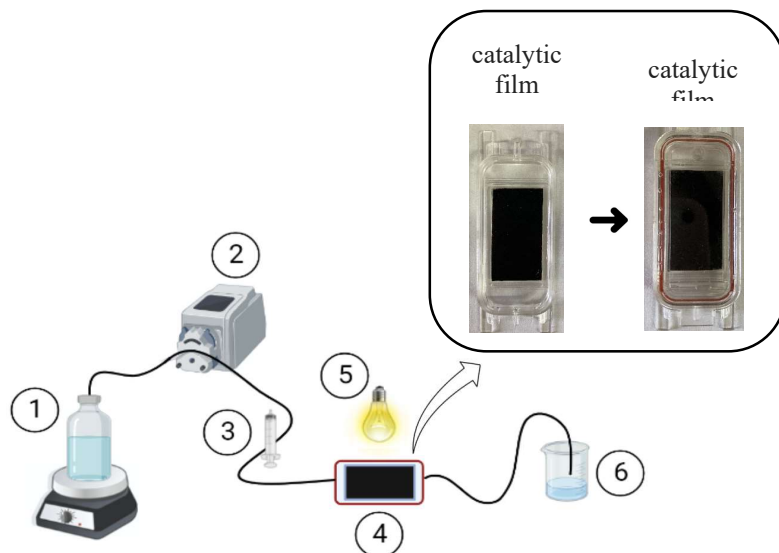


**Fig. S1.** Schematic representation of the experimental arrangement used for IMD degradation: (1) reservoir containing the pesticide and PMS, (2) peristaltic pump, (3) bubble trap, (4) catalytic film + flow cell (7.7 cm<sup>3</sup>, Sigma-Aldrich), (5) Xe arc lamp (15 cm above the flow cell), and (6) reservoir for the treated solution.

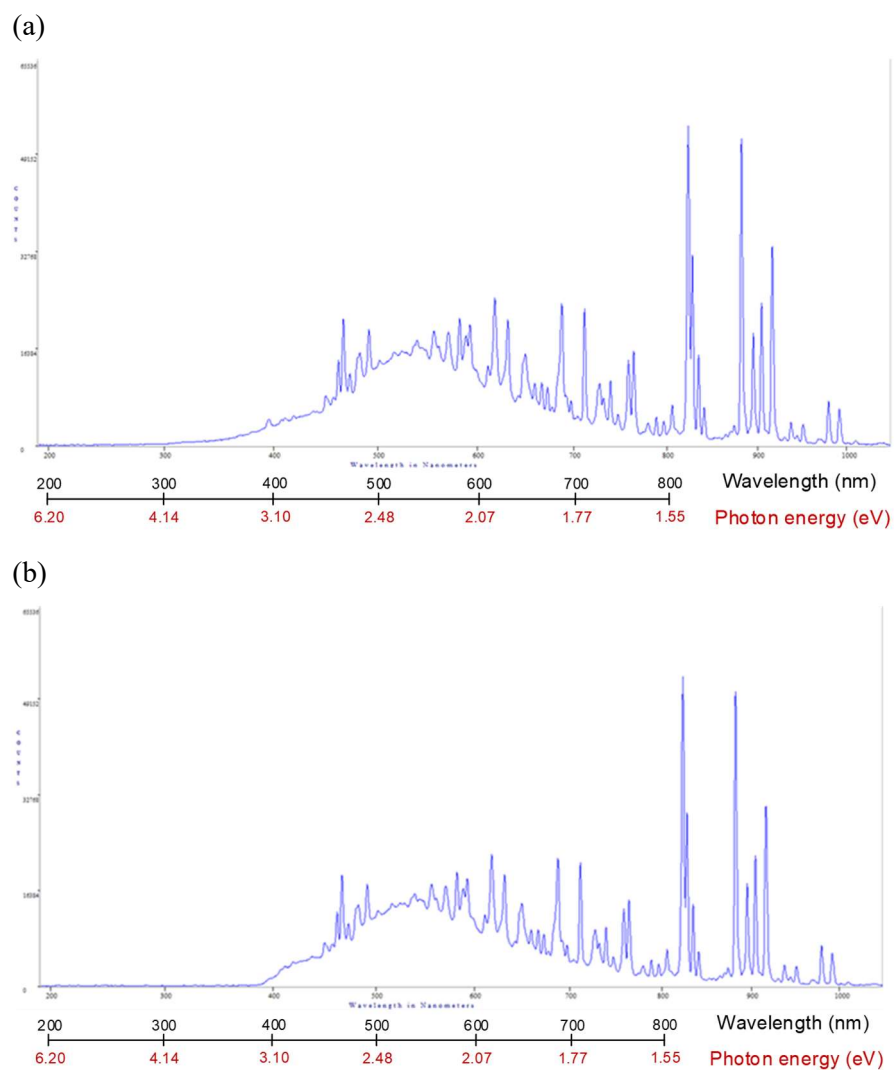


**Fig. S2.** Emission spectra of the Heraeus TQ 150 Xe arc lamp (a) and the Heraeus TQ Xe arc lamp with R3114 UV filter (b).

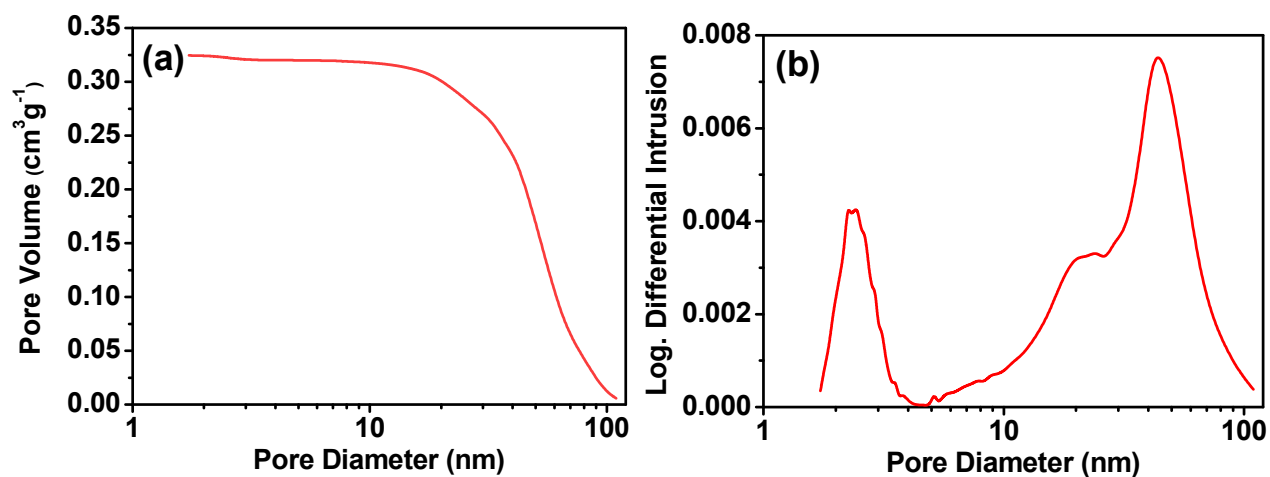


**Fig. S3.** Cumulative pore volume (a) and pore size (b) distributions of the as-synthesized  $\text{Co}_3\text{O}_4$  nanoparticles.

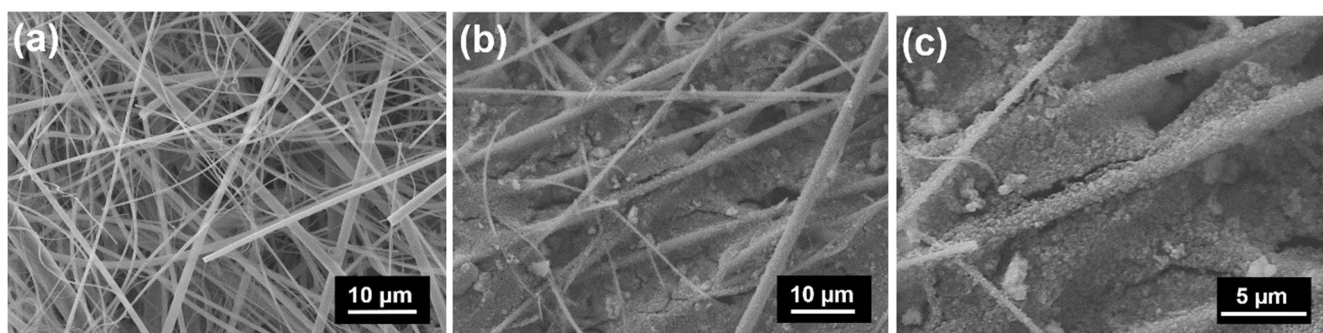


**Fig. S4.** Top-view SEM images of the glass microfiber filter substrate (a) and the  $\text{Co}_3\text{O}_4$ -coated substrate fabricated by vacuum filtration (b-c).